SOLUTION MINING RESEARCH INSTITUTE

679 Plank Road
Clifton Park, NY 12065, USA

Telephone: +1 518-579-6587
www.solutionmining.org

Technical Conference Paper

On the generation of 3D Microstructural Models to Analyze Creep and Permeation Behavior though Digital Twin Simulations

Joyce Schmatz, Eva Wellmann, Mingze Jiang
Microstructure and Pores GmbH, Aachen, Germany
Tobias Baumann
smartTectonics GmbH, Mainz, Germany
Benoit Brouard
Brouard Consulting, Paris, France
Richard R. Bakker, Marinus den Hartogh
Nobian Industrial Chemicals B.V., Amersfoort, The Netherlands

SMRI Spring 2025 Technical Conference
27-29 April 2025
Wilhelmshaven, Germany

Solution Mining Research Institute Spring 2025 Conference

Wilhelmshaven, Germany, 27-29 April 2025

On the generation of 3D Microstructural Models to Analyze Creep and Permeation Behavior though Digital Twin Simulations

Joyce Schmatz[1], Eva Wellmann[1], Mingze Jiang[1], Tobias Baumann[2], Benoit Brouard[3], Richard R. Bakker[4], Marinus den Hartogh[4]

[1]Microstructure and Pores GmbH, Junkerstraße 93, 52064, Aachen, Germany
[2]smartTectonics GmbH, Im Niedergarten 18, 55124 Mainz, Germany
[3]Brouard Consulting, Paris, France
[4]Nobian Industrial Chemicals B.V., Van Asch van Wijckstraat 53, 3811 LP Amersfoort, The Netherlands

Abstract

This study presents the development of three-dimensional (3D) input datasets of natural rock salt at the laboratory scale, intended to support digital twin simulations of creep and permeation behavior. These simulations aim to improve the interpretation of experimental results and facilitate more reliable upscaling to reservoir-scale conditions. The 3D digital twin models introduced here account, for the first time, for internal grain size variations, providing a more realistic representation of sample heterogeneity to support advanced simulation workflows.

Natural rock salt exhibits significant heterogeneity in grain size and impurity content, further complicated by artifacts introduced during coring and laboratory preparation. Understanding how this heterogeneity influences deformation and fluid transport remains a key challenge.

Core samples from a Danish salt diapir were analyzed using multiscale imaging techniques, including reflected-light microscopy, slab-scale imaging in 2D, and 3D micro-computed tomography (CT). Grain sizes were quantified using semi-automated segmentation of thin sections and slab photographs, as well as a machine learning-based classification of CT data. A random forest classifier was trained on the basis of 2D data to segment CT volumes into distinct grain size classes and anhydrite-rich phases. Creep and permeation test results were linked to the internal grain size distributions of each sample.

Grain sizes measured from thin sections aligned well with creep rates predicted by established pressure solution creep laws, whereas coarser-grain estimates from CT and slab analyses underestimated deformation rates, likely due to unresolved fine grains or the passive role of large grains. In permeation tests, samples with larger grain sizes and mega-grain inclusions exhibited increased fluid transport, suggesting reduced healing efficiency and enhanced flow along coarse-grain boundaries.

Notably, discrepancies between 2D and 3D grain size estimates – particularly in samples exhibiting pronounced layering or coarse-grained facies with tabular-shaped grains – underscore the importance of considering spatial heterogeneity and directional textural variation when interpreting the mechanical and transport behavior of rock salt.

This study emphasizes the necessity of accurately capturing microstructural heterogeneity in digital models to better understand the mechanical and hydraulic response of rock salt. The generated 3D datasets serve as a foundational resource for future digital twin simulations, which will explore how internal grain size variation and structural anisotropy influence localized deformation and fluid flow.

Key words: rock salt, 3D digital twin models, digital rock physics, grain size facies, 3D anisotropy

1. Introduction

The objective of this study is to generate laboratory-scale, three-dimensional input datasets of natural rock salt for integration into digital twin simulations. These simulations are designed to analyze creep and permeation behavior at the sample scale (see Baumann et al., this issue), serving as benchmarks for experimental procedures and enhancing the interpretation of laboratory test results (Schmatz et al., 2024, Hermann et al., in press, Schmatz et al., in press).

Natural rock salt exhibits inherent heterogeneity due to variations in impurity content and grain size distribution (e.g., Ter Heege et al., 2005, Schwichtenberg et al., 2022, Schmatz et al., 2024). Additionally, subsurface core samples often develop artifacts such as microcracks and dilated grain boundaries caused by stress relaxation, as well as dissolution features resulting from exposure to drilling fluids. During laboratory testing, these samples undergo geometric modifications influenced by experimental conditions and the activation of microphysical processes. Interpreting test results remains challenging due to the limited understanding of stress-strain localization mechanisms and their interaction with permeation pathways in heterogeneous salt matrices.

Digital rock physics (Andrä et al., 2013a and Andrä et al., 2013b) offers a promising approach to overcoming these challenges by enabling the detailed analysis of internal sample structures, which are otherwise difficult to monitor in standard laboratory setups. It allows for the simulation of various reservoir conditions (e.g., different pressures, fluid types) without physically altering the sample and is particularly useful when physical core samples are limited or unavailable. By integrating digital twin simulations at the core scale with pore-scale and field-scale data, digital twins can support a comprehensive upscaling approach, bridging the gap between laboratory experiments and reservoir-scale processes (Noiriel and Soulaine, 2021).

Several approaches have been employed to characterize the three-dimensional, spatially resolved deformation and permeation behavior of rock salt. These methods include acoustic emission measurements to localize the initiation of brittle deformation (Manthei, 2005; Li et al., 2019), four-dimensional in-operando X-ray tomography to monitor strain localization in real time (Schwichtenberg et al., 2022), and post-mortem CT investigations to analyze permeation behavior following deformation (Zhang et al., 2020; Schmatz et al., 2024), among other advanced imaging techniques.

However, investigating grain boundary-scale processes, such as dissolution-precipitation during pressure solution creep, requires extremely small specimens to achieve the spatial resolution necessary for detailed analysis. As a result, to accurately visualize individual grain boundaries, sample dimensions must be reduced to the millimeter scale (e.g., Thiemeyer et al., 2015; Ji et al., 2022), which in turn complicates upscaling due to the limited representativeness of such small-scale measurements.

The deformation and permeation behavior of heterogeneous rock salt has been extensively studied for decades and results demonstrate that creep behavior in the pressure solution creep regime, as well as permeation along microcracked grain boundaries, is strongly governed by grain size (e.g., Urai et al., 1986, Spiers at al., 1990, Schulze et al., 2001, Popp et al., 2015, Urai et al., 2019). In natural rock salt, grain size variation can be extreme, with alternating layers of fine-grained matrix halite (sub-millimeter scale) interspersed with halite mega-grains – tabular grains reaching sizes in the decimeter- to meter-scale (Barabasch et al., 2023, Küsters et al., 2008). Commonly, when testing natural rock salt using standard laboratory core cylinders (5–10 cm diameter), these grain size variations may affect the representativeness of the sample material and complicate the interpretation of bulk strain and permeation behavior. Paterson and Wong (2005) advise that the smallest dimension (radius of the test cylinder) should exceed the largest grain by a factor of 10. However, due to the possible presence of mega-grains or large second phase inclusions this is not always feasible in common laboratory settings.

The 3D digital twin models presented in this study account, for the first time, for internal grain size variations and are designed to support digital twin simulations. These simulations aim to more accurately constrain local microphysical processes, thereby enabling more reliable upscaling of creep and permeation test results. A comparison with laboratory test data provides an initial evaluation of the impact of a heterogeneous grain size distribution within a test specimen on the outcomes of both creep and permeation experiments. Digital twin simulations based on the presented 3D models, replicating the conditions of the physical creep tests, are the focus of a complementary study by Baumann et al. (this issue).

2. Samples

The samples used in this study originate from core material extracted from a salt diapir in the Northern Permian Basin in Denmark. Prior to laboratory testing and CT scanning, which served as the basis for the 3D models, the samples were cut and ground to the required dimensions: approximately 60 mm (2.36”) in diameter and 120 mm (4.72”) in length for permeation tests (Schmatz et al., 2024), and 70 mm (2.76”) in diameter and 140 mm (in 5.51”) length for creep tests (Baumann et al., 2022, Schmatz et al., in press).

After testing, the cylindrical specimens were sawn in half along the long axis and perpendicular to macroscopically visible planes, which could indicate bedding, creating slab sections. From one slab of each sample, thin sections, measuring ~50 mm × 70 mm (1.97” × 2.76”) with a thickness of ~1 mm (0.04”), were prepared from the center of the sample for microstructural analysis.

In total, four 3D models were generated: two models from creep-tested samples (sample IDs: 01_m1 and 06_m1), and two models from permeated samples (sample IDs: 01_p1 and 04_p1).

3. Methods

Grain size measurement at the thin section scale

Reflected-light micrographs with a pixel resolution of 3.45 µm (4e-5”) were utilized to determine the grain size of matrix grains within thin sections. To enhance grain boundary visibility, thin-section surfaces were etched following the protocol outlined by Urai et al. (1987). This process involved immersing polished thin sections in slightly undersaturated NaCl-brine for 8–13 seconds, followed by brine removal using pressurized air.

Grain size determination (Figure 1) was performed using a semi-automatic segmentation tool designed for the rapid manual segmentation of grains from reflected-light micrographs of the etched surfaces. Grain size was quantified using the equivalent circular diameter (d). Most grain boundaries and individual grains contained secondary phases, such as fluid inclusions and small anhydrite grains or grain clusters. The segmentation algorithm was specifically developed to exclude secondary phases located at grain boundaries while retaining those within grains as part of the measured grain area. Additionally, grains intersecting the image or thin-section edges were excluded from the analysis to ensure accurate size measurements.

Grain size model at the slab scale

Core-piece slabs were analyzed to quantitatively assess the degree of heterogeneity within various rock salt lithofacies. To account for this heterogeneity, the microstructure was first examined using transmitted and reflected light flatbed scans of core-piece slabs, which were cut from the center of each core parallel to the long axis. These scans were acquired at a pixel resolution of 10 µm. The observed heterogeneity was primarily attributed to local variations in grain size, often associated with subvertical layering and variable second-phase dust content. This dust consisted of micron-sized inclusions, commonly consisting of anhydrite and polyhalite, dispersed along halite grain boundaries.

To quantify grain size variations at the slab scale, we applied a grain size classification scheme for polycrystalline rocks, following Kozlov et al. (2006) (Figure 2(1)), based on visual inspection of slab surfaces. Grain size classes were defined by their minimum and maximum d values (Figure 2(1)). However, at the thin-section scale, grain size distributions typically follow a log-normal pattern (Figure 1 and Figure 2, Ter Heege et al., 2005). To model these distributions, we calculated log-normal distributions for all grain size classes using the observed minimum and maximum grain size values. This calculation assumes a variability range expressed through different standard deviations (σ = 0.005–1, Figure 2(3)), applying the following equations:

Eq.1:

$$\mu = \frac{\ln(\min d) + \ln\,(\max d)}{2}$$

Eq. 2:

$$\sigma = \frac{\ln(\min d) + \ln\,(\max d)}{2\mathrm{z}}$$

With µ: mean, σ: standard deviation, min d: minimum grain size value, max d: maximum grain size value, and z: z-value of the 99% quantile of the standard normal distribution.

To quantitatively describe the spatial distribution of grain size classes, slabs were manually segmented into distinct grain size class areas (Figure 2(4)). This segmentation process involved comparing transmitted and reflected light photographs of the slabs with the corresponding physical samples and thin-section images. The segmentation results were independently reviewed by two experts to ensure accuracy. The relative distribution of grain size classes (Figure 2(5)) was then used to compute the average grain size of each slab, based on the theoretical log-normal distribution of the grain size classes (Figure 2(6)). An example of slab segmentation and grain size class distribution for core piece 01_s1, a sister sample representing the initial state of samples 01_m1 and 01_p1, is provided in Figure 12(4).

It is important to note that macroscopic investigations tend to overestimate grain size due to the optical properties of grain boundaries, which can obscure smaller grains. Consequently, very small grains may be overlooked in such analyses.

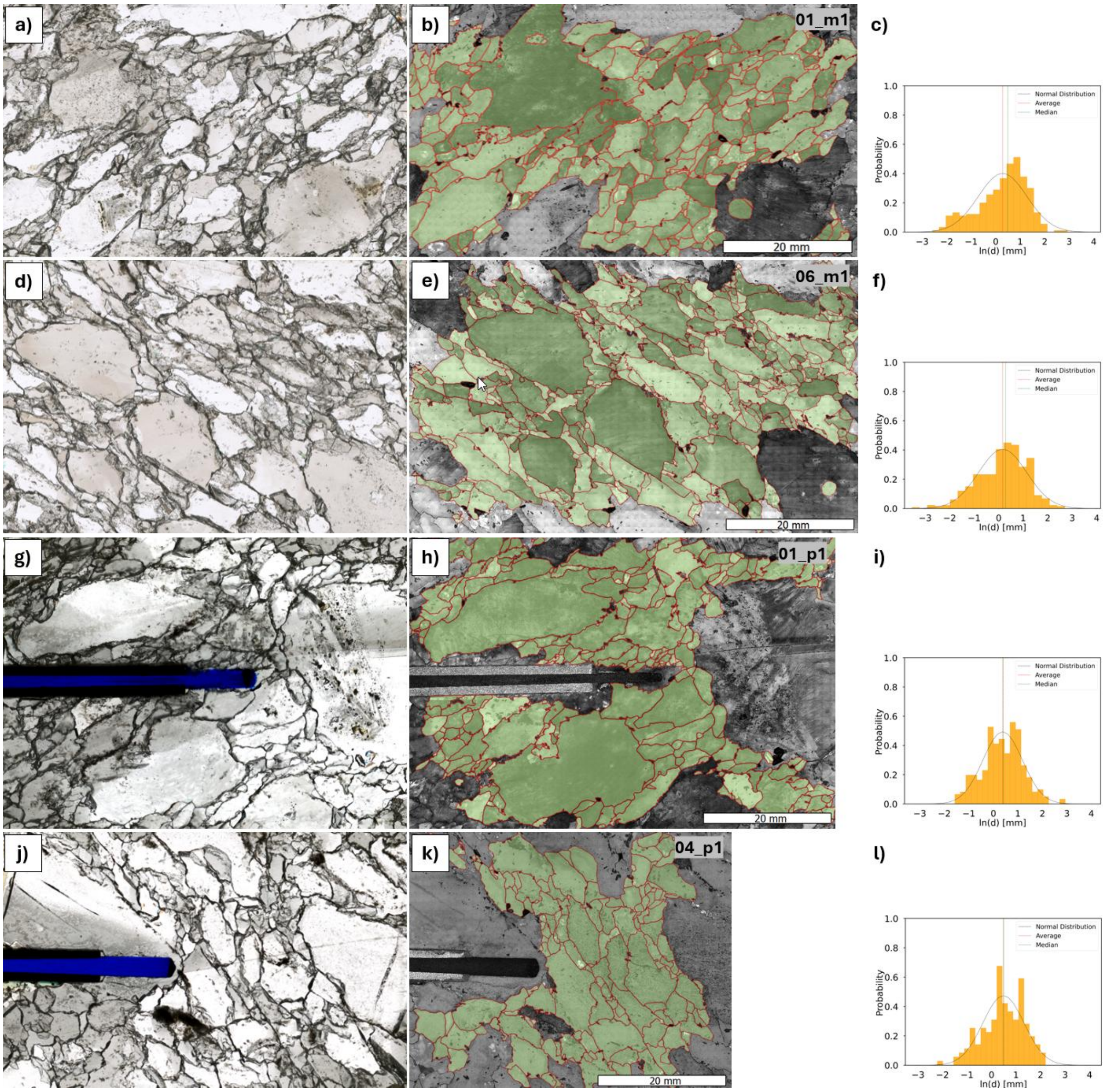

Figure 1. Grain size measurements at the thin-section scale. Panels a), d), g), and j) show the thin sections of samples 01_m1, 06_m1, 01_p1, and 04_p1, respectively. Panels b), e), h), and k) present the corresponding grain size measurements obtained from reflected light micrographs. Panels c), f), i), and l) display the associated grain size distributions in the form of histograms.

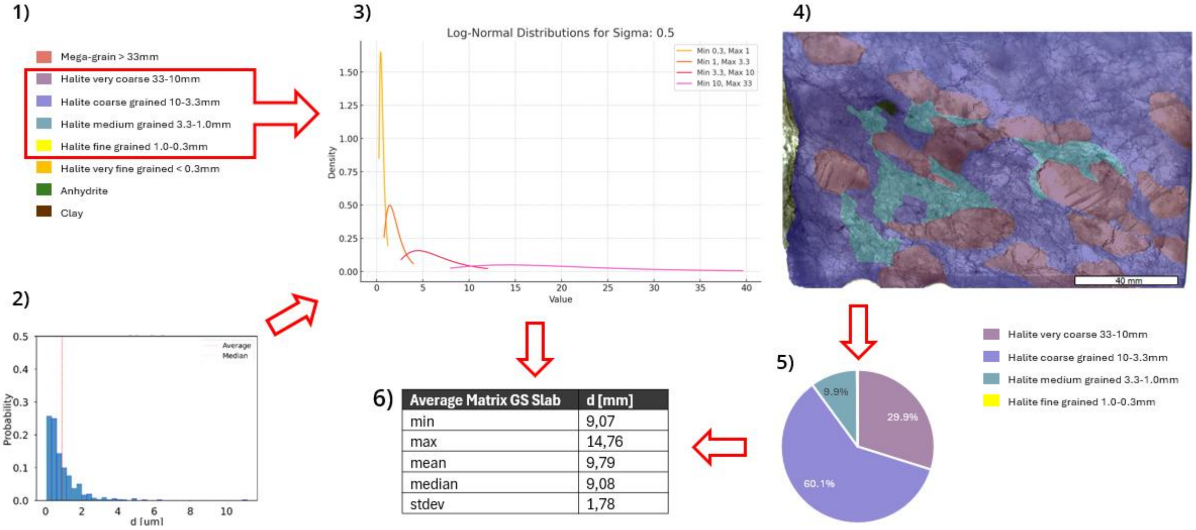

Average Matrix GS Slab	d [mm]
min	9,07
max	14,76
mean	9,79
median	9,08
stdev	1,78

Figure 2. Grain size model at the slab scale. The visualization illustrates the spatial distribution of grain size classes across the slab surface. For details on the segmentation methodology, grain size classification, and interpretation, refer to the main text.

3D digital twin model

All samples were scanned in three dimensions using micro-computed tomography (micro-CT) with a Nikon METRIS 3 X-TEK XT H 320 LC scanner with voxel sizes of 85 µm (3.4e-3”) for samples 01_m1 and 06_m1, and 74 µm (2.91e-3”) for samples 01_p1 and 04_p1.

Several post-processing steps were required to enhance the visualization of features of interest. The raw imagery, consisting of 32-bit float data, was provided in .vol file format and imported into Fiji (https://imagej.net/software/fiji/) for further processing. Initially, the data were cropped to isolate the sample volume. If a noticeable radial gradient was present, it was identified and subtracted from the original dataset using mathematical operations. Contrast enhancement was then applied to facilitate the identification of fractures, pores, and anhydrite. Finally, these features were analysed using 3D filtering, local thresholding, and noise removal to quantify their proportions and visualize their spatial interactions.

Following the principle that fine-grained sample volumes, which have a higher density of grain boundaries, typically exhibit lower overall densities than coarse-grained volumes, we identified different grain size classes by analysing contrast variations (pixel variance) in the CT data (Figure 3). Additionally, the presence of fine, dispersed second-phase dust (anhydrite) along grain boundaries served as an indicator of grain size class, with higher dust concentrations corresponding to smaller grain sizes.

Since grain size classes could not be reliably determined by thresholding voxel grey values, due to the low signal-to-noise ratio in the CT data, a machine learning algorithm based on random forest classification was employed to segment the 3D volume according to grain size classes. A random forest classifier (e.g., Breiman, 2001) is an ensemble learning method composed of multiple decision trees, each trained on a random subset of the training data. These trees independently predict the class label, and their outputs are aggregated to produce a more accurate and stable classification. To generate the training dataset, approximately 100 sample patches per grain size class were manually labelled. This classification process was supported by manual ground truth preparation, which involved the segmentation of individual grain size classes in selected 2D CT slices, combined with insights from previously classified sample slabs (Figures 6-10). Resulting digital models categorized the halite matrix into three distinct grain size classes, alongside the anhydrite phase, which was identified through local thresholding. The average grain size on the sample scale was computed from the relative phase distribution using the same schema as described above for the 2D grain class distribution derived from the slab segmentation.

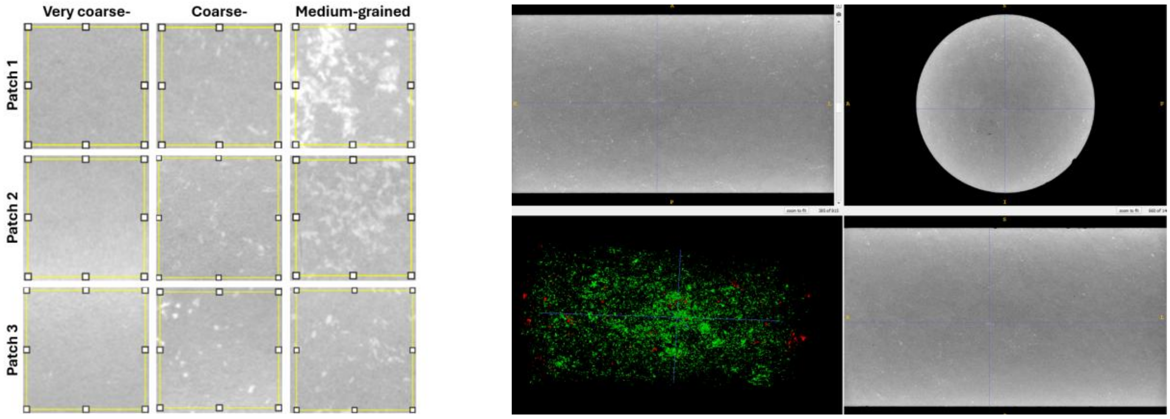

Figure 3. 3D CT Model training data. Left: sample patches for the different grain size classes. Right: raw CT scan slices from 3 orthogonal sides in the centre of the core piece cylinder 01_m1 with the 3D segmentation result for second phase anhydrite (green) and pores (red) in the lower left.

Creep Tests

Between 2014 and 2016, an experimental program (Bérest et al., 2017, 2019, 2022) supported by the SMRI demonstrated that, within the 0.2–1 MPa (29-145 psi) deviatoric stress range, natural rock salt creeps at rates several orders of magnitude faster than those extrapolated from standard laboratory tests conducted at 5–20 MPa (725-2900 psi). Following this protocol, uniaxial creep tests were performed in a mine gallery under controlled environmental conditions to minimize strain fluctuations caused by external factors. The gallery maintained a stable temperature of 8 °C (46.4 °F, with annual variations ≤0.01 °C) and a relative humidity of 67.3 (with fluctuations ≤0.5% RH). Creep tests were conducted on samples 01_m1 and 06_m1, using dead weights to ensure consistent stress application. The samples were positioned between duralumin plates, and stress was calculated based on their initial cylinder dimensions. The applied stress levels were 0.6 MPa (87 psi) for sample 06_m1 and 3.0 MPa (435 psi) for sample 01_m1 (Figure 4). Prior to testing, both samples underwent hydrostatic preconditioning at 90 °C (194 °F) and 20 MPa (2900 psi) for approximately 80 hours. To ensure brine saturation within the sample assembly before preconditioning, the samples were encased in an elastomer jacket, and saturated NaCl brine was introduced. Further details on the test protocol and microstructural assessment can be found in Schmatz et al. (in press).

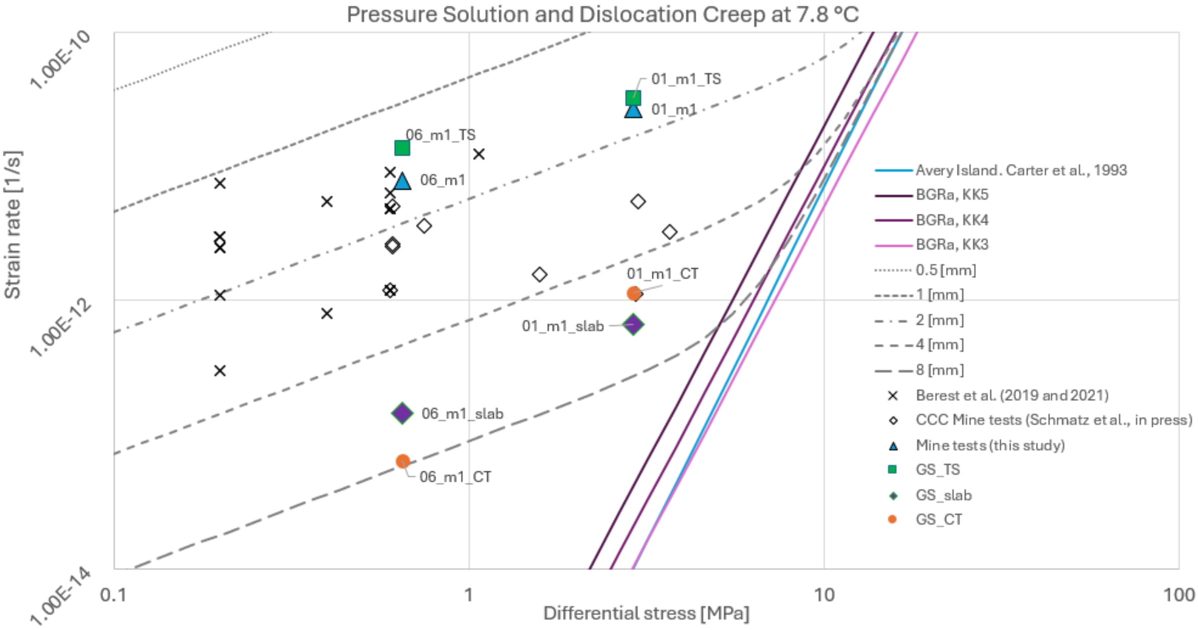

Figure 4. Result uniaxial creep test with strain rates for thin section (_TS), slab, and CT segmentations calculated after Spiers et al. (1990).

Permeation Test

Permeation tests were conducted at the IfG – Institut für Gebirgsmechanik in Leipzig, Germany, using hydraulic creep apparatuses equipped with a triaxial cell, following the methodology of Popp et al. (2015) with two key modifications: 1. a small differential stress was applied to simulate a non-isotropic stress state at a cavern wall and 2. saturated brine was used instead of inert gas as the permeating fluid, representative for the abandoned cavern case and allowing for possible fracture healing through brine precipitation. Cylindrical samples (01_p1 and 04_p1) were encased in rubber jackets to isolate pore pressure from the hydraulic oil. The experiments were conducted at 40 °C ± 0.2 (104 °F), with prior calibration ensuring an equal temperature in the whole sample. Radial stress (i.e., confining pressure) was maintained at 15 MPa (2175 psi), and an initial isostatic stress phase facilitated sample compaction before increasing the axial stress to a differential stress of 1 MPa (145 psi).

Permeation tests lasted 30–50 days, during which axial displacement was continuously logged to develop a stress-strain curve. However, achieving a steady-state strain rate within this timeframe was unlikely (Figure 5). A 3 mm borehole, sealed with an epoxy-cemented metal rod, created a miniature cavern ("mini-cavern") within each sample. Brine injection induced radial flow, which exited through a porous mesh and sintered filter plate. A Quizix® syringe pump-controlled injection pressure and adjusted flow rates, automatically stopping at excessive flow (indicating some permeable pathway has formed) and subsequently pressure decay monitoring. To maintain full brine saturation, the brine passed through a salt powder reservoir before injection. Real-time data monitoring enabled efficient experiment management.

Upon breakthrough at high pressures, injection was automatically halted, allowing for potential fracture healing before increasing pressure again to further investigate permeation behaviour.

Further details on the test protocol and microstructural assessment can be found in Schmatz et al. (2024) and Hermann et al. (in press).

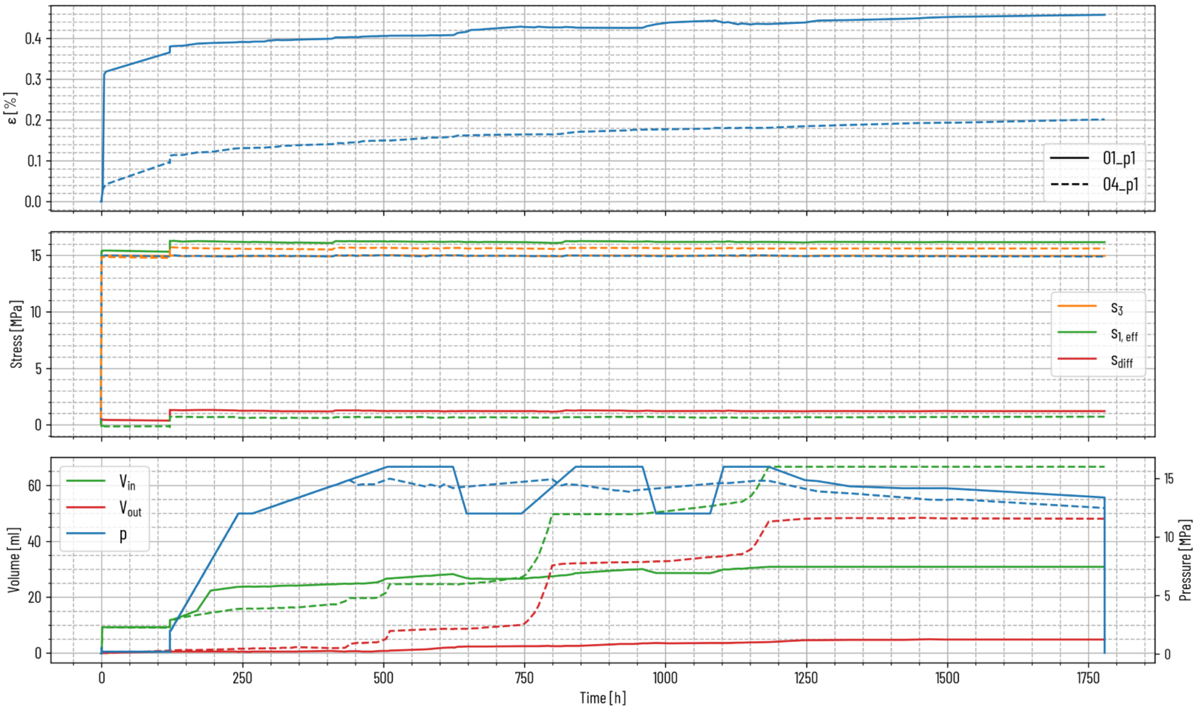

Figure 5. Permeation test results. For details on the methodology, results, and interpretation, refer to the main text. (See the main text for English units).

4. Results and Discussion

3D models creep tests

Both the manual slab photograph segmentation and the 3D segmentation of the CT scan yield relatively similar average grain sizes for the creep-tested sample 01_m1 (Figures 6 and 10), with values of 6.32 mm (0.25”) (Std. Dev. = 1.18 mm (0.05”)) for slab segmentation and 5.30 mm (0.21”) (Std. Dev. = 0.99 mm (0.04”) for CT segmentation. In contrast, for sample 06_m1 (Figures 7 and 10), a significant discrepancy of approximately 2 mm (0.08”) is observed between the 2D and 3D segmentation results, with an average grain size of 6.39 mm (0.25”) (Std. Dev. = 1.19 mm (0.5”)) from slab segmentation and 8.38 mm (0.33”) (Std. Dev. = 1.55 mm (0.06”)) from CT segmentation.

Assuming a homogeneous medium, stereological principles (e.g., Underwood, 1970) would permit a direct extrapolation from 2D to 3D for a cylinder without additional correction factors. However, the pronounced difference in 2D versus 3D segmentation for sample 06_m1 is primarily attributed to a greater abundance of the very coarse-grained fraction, which occurs in regular, gently tilted layers interspersed with finer-grained facies. This results in a highly anisotropic 3D texture that cannot be fully represented within a single 2D slice. Conversely, in sample 01_m1, the very coarse-grained facies are spatially confined within the sample volume, embedded in alternating layers of finer-grained facies. The overall finer-grained matrix does not produce significant anisotropy due to the limited lateral extent of medium-to-coarse grains in the z-direction.

For both samples, the average matrix grain size obtained from thin-section segmentation (Figure 1) is relatively similar: 1.99 mm (0.08”) (Std. Dev. = 2.70 mm (0.11”)) for sample 01_m1 and 1.79 mm (0.07”) (Std. Dev. = 2.86 mm (0.11”) for sample 06_m1. It is important to note that the grain size measurements obtained from thin-section reflected-light micrographs, with a pixel resolution of 3.45 µm (4e-5”), are substantially more accurate than those derived from slab images. This is primarily due to the threefold higher pixel resolution of thin-section images and the enhanced visibility of grain boundaries facilitated by surface etching and the optics of a 10X objective lens. In contrast, slab image segmentation based on a visual inspection of transmitted light photographs may overlook very small grains and tightly bound grain boundaries. However, in heterogeneous rock salt, the thin-section dimensions may not be fully representative of the overall grain size distribution, particularly if the rock contains abnormally large grains exceeding several centimeters in diameter.

A strain rate versus stress diagram (Figure 4) comparing the creep test results with previous experiments clearly indicates that the dominant deformation mechanism is linear pressure solution creep, governed by dissolution-precipitation processes. This allows for a direct comparison using the creep law established by Spiers et al. (1990). When calculating the strain rate based on the average grain size and applying this creep law, a strong agreement is observed for the grain size derived from thin-section segmentation (01_m1_TS and 06_m1_TS, Figure 4). However, the strain rates computed using grain size data from slab (01_m1_slab and 06_m1_slab, Figure 11) and CT (01_m1_CT and 06_m1_CT, Figure 11) segmentation are more than two orders of magnitude slower than the predictions from Spiers et al. (1990).

Several potential explanations exist for this discrepancy. One possibility is that the grain size obtained from slab and CT segmentation significantly overestimates the actual mean grain size, as a substantial number of smaller grains may be overlooked due to their size and the optical properties of tightly bound grain boundaries. Alternatively, it is plausible that creep is predominantly controlled by the smallest grain size fraction, corresponding to the medium-sized grains measurable at the thin-section scale, while larger grains behave as passive inclusions with minimal contribution to the overall creep rate due to their relatively low surface-area-to-volume ratio. To further investigate these mechanisms, digital twin simulations that incorporate grain boundary processes alongside local stress–strain relationships offer valuable insights into the factors controlling creep rates in heterogeneous rock salt (e.g., Ma et al., 2023). Kottwitz et al. (in press) and Baumann et al. (this issue) test the first of these hypotheses that grain size is overestimated on the slab scale by conducting simulations in which the grain size class is reduced by one category. This adjustment leads to a plausible match between simulated and actual laboratory creep results, supporting the hypothesis.

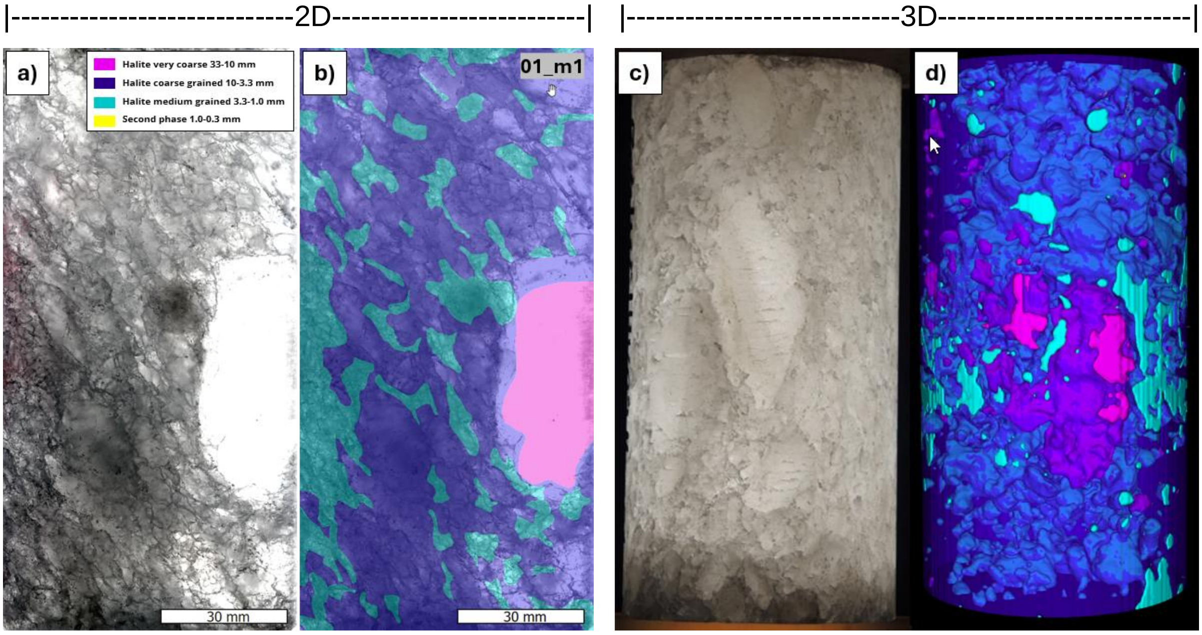

Figure 6. Segmentation result creep test sample 01_m1. a) transmitted light scan slab, b) 2D segmentation scan (see a) for legend), c) transmitted light photograph test cylinder (diameter is 70 mm), and d) 3D model (see a) for legend).

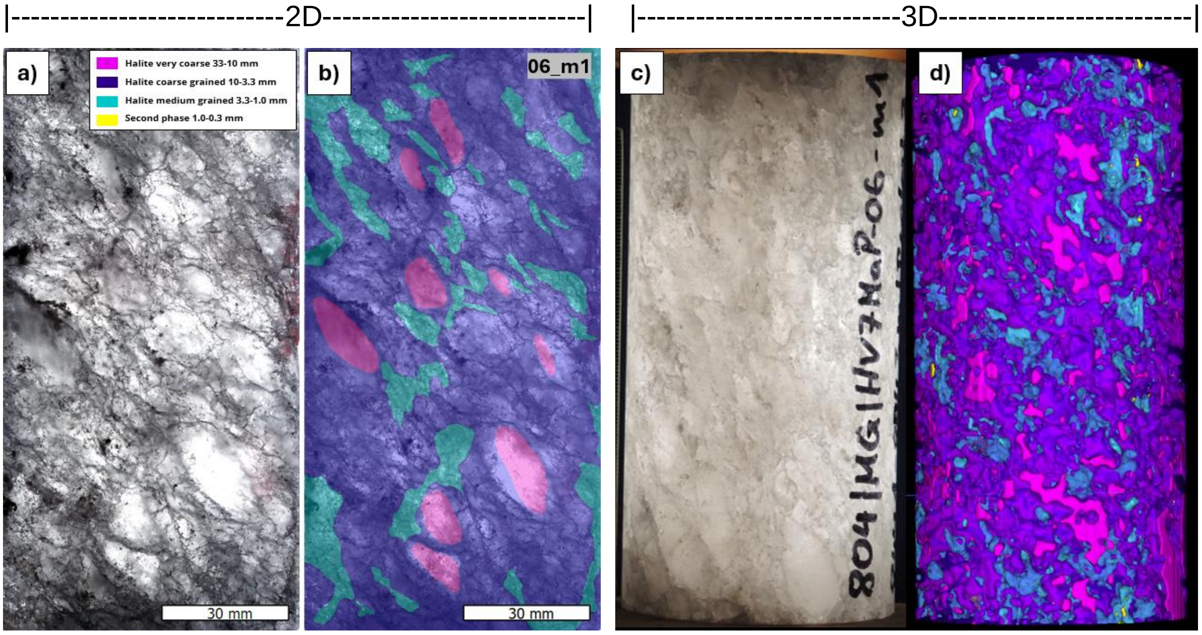

Figure 7. Segmentation result creep test sample 06_m1. a) transmitted light scan slab, b) 2D segmentation scan (see a) for legend), c) transmitted light photograph test cylinder (diameter is 70 mm), and d) 3D model (see a) for legend).

3D models permeation tests

The overall observations regarding the rock fabric in the 3D models used for permeation tests are largely consistent with those used for uniaxial creep tests. Both manual slab photograph segmentation and 3D CT scan segmentation yield comparable average grain sizes for the creep-tested sample 01_p1 (Figures 8, 10, and 11), with values of 7.38 mm (0.29”) (Std. Dev. = 1.37 mm (0.05”)) from slab segmentation and 6.99 mm (0.28”) (Std. Dev. = 1.30 mm (0.05”)) from CT segmentation. For sample 04_p1 (Figures 9, 10, and 11), a noticeable discrepancy of approximately 1 mm (0.04”) is observed between 2D and 3D segmentation results, with an average grain size of 7.02 mm (0.28”) (Std. Dev. = 1.30 mm (0.05”)) from slab segmentation and 8.14 mm (0.32”) (Std. Dev. = 1.50 mm (0.06”) from CT segmentation. The difference between 2D and 3D models in this sample is primarily attributed to its more pronounced anisotropy, which is associated with the presence of the layered, very coarse-grained facies. In contrast, the layering in sample 01_p1 is predominantly controlled by finer-grained facies and abundant anhydrite dust, resulting in less anisotropy in the third dimension compared to the tabular, very coarse grains present in sample 04_p1.

Similarly, in the permeation samples, the 2D matrix grain size measured from etched thin-section surfaces is comparable between both samples, with values of 2.03 mm (0.08”) (Std. Dev. = 2.34 mm (0.09”)) for sample 01_p1 and 2.22 mm (0.09”) (Std. Dev. = 2.32 mm (0.09”)) for sample 04_p1.

The sister samples 01_m1 and 01_p1 exhibit a similar trend across all three segmentation methods. However, sample 04_p1 shows an approximately 1 mm (0.4”) larger average grain size for the 2D slab and 3D CT segmentations, which can be attributed to a higher abundance of very coarse-grained inclusions within the test cylinder compared to sample 01_m1.

Figure 10 presents a close-up view of the central region of the permeation samples, with a semi-transparent visualization of the different grain size facies and the tubing with the mini-cavern at the centre. In both samples, the mini-cavern is positioned centrally, ensuring contact with all three grain size classes.

Both permeation samples (01_p1 and 04_p1) exhibit similar permeation behaviour (Figure 5), characterized by an initial breakthrough occurring within the first few days of testing. However, after a short healing period and a gradual, stepwise increase in fluid pressure, brine breakthrough reoccurs once the pore fluid pressure reaches the minimum principal stress. Sequential healing cycles allowed for the repeated triggering of multiple breakthroughs. The primary difference between the permeation behaviour of the two samples lies in the total volume of brine permeated at comparable pore fluid pressures. Specifically, the volume of brine permeated through sample 04_p1 is approximately twice as large as that of sample 01_p1. This discrepancy may be influenced by microstructural factors, particularly grain size and the distribution of second-phase dust: Sample 04_p1 exhibits an overall larger grain size and a higher proportion of very coarse grains. According to Schmatz et al. (2024), grain boundary healing (Houben et al., 2013) is less effective along the boundaries of very large grains (mega-grain (-remnants)), potentially resulting in more sustained permeation and localized fluid flow along these boundaries. Additionally, sample 04_p1 contains layers of medium-grained halite interspersed with millimetre-sized anhydrite inclusions and finely dispersed second-phase dust. These layers may introduce a form of mechanical stratigraphy, which could further influence permeation behaviour by promoting or restricting fluid flow along specific structural planes.

Future digital twin simulations will address the effect of internal heterogeneity on local variations in pore pressure and fluid flow within permeated specimens. While the digital creep test presented in Baumann et al. (this issue) is based on our CT-scanned data, upcoming simulations will extend the digital twin framework to incorporate a mini-cavern geometry and include time-dependent boundary conditions from the physical permeation experiments—such as applied load and fluid pressure—to mimic their real-world counterparts. This will allow for a detailed investigation of the interplay between local stress distribution, fluid–solid coupling, and pressure-driven permeation, influenced by second-phase impurities and segmentation geometries derived from microstructural characteristics. The results are expected to provide important insights for cavern abandonment scenarios.

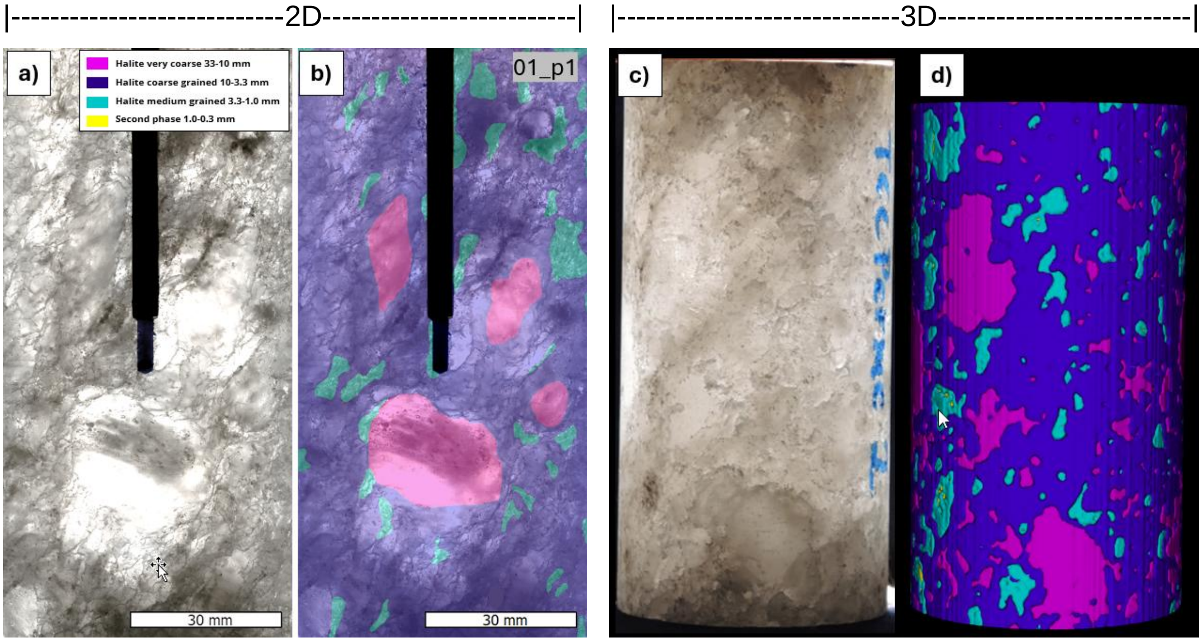

Figure 8. Segmentation result creep test sample 01_p1. a) transmitted light scan slab, b) 2D segmentation scan (see a) for legend), c) transmitted light photograph test cylinder (diameter is 60 mm), and d) 3D model (see a) for legend).

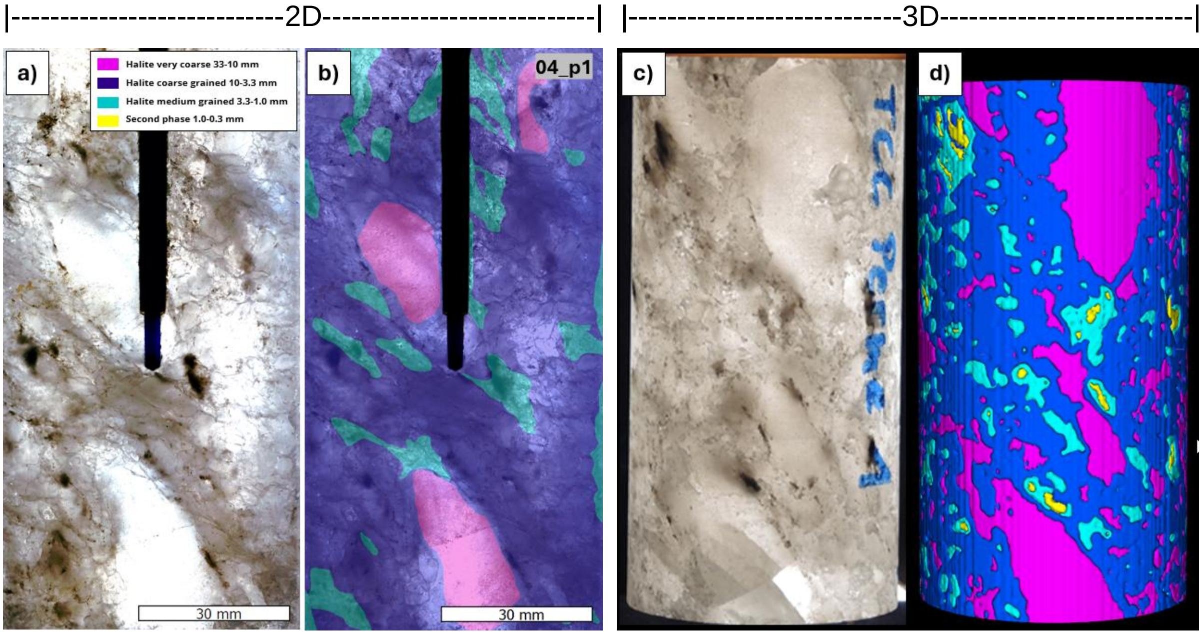

Figure 9. Segmentation result creep test sample 04_p1. a) transmitted light scan slab, b) 2D segmentation scan (see a) for legend), c) transmitted light photograph test cylinder (diameter is 60 mm), and d) 3D model (see a) for legend).

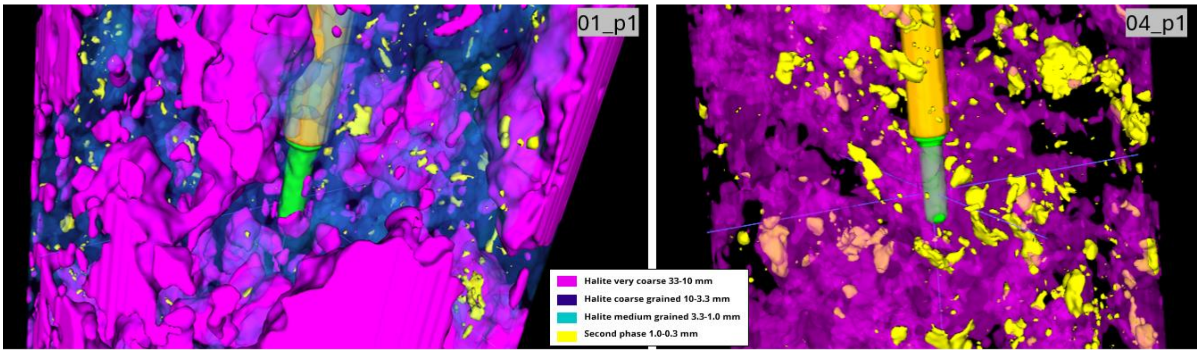

Figure 10. Close-up, 3D visualisation with semi-transparent overlay of the segmented grain size classes and the tubing (orange) and the min-cavern (green) in the centre of the test cylinder.

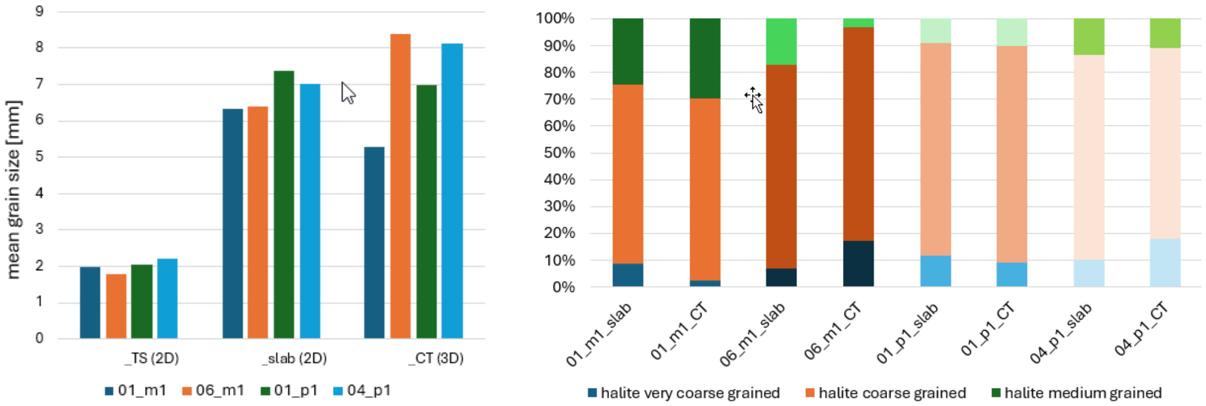

Figure 11. left: average grain size from thin section (TS), slab, and CT segmentation, right: grain size class fraction from slab and CT segmentation. (See the main text for English units).

5. Concluding Remarks

The integration of 2D and 3D segmentation techniques across both creep and permeation test samples provides a comprehensive assessment of grain size distributions and their implications for deformation and fluid transport in heterogeneous rock salt. While thin-section analysis offers high-resolution insights into matrix grain size, slab and CT-based segmentations capture larger-scale structural features and highlight anisotropies not visible in 2D sections alone. Notably, discrepancies between 2D and 3D grain size estimates, particularly in samples with pronounced layering or coarse-grained facies, underscore the importance of considering spatial heterogeneity and directional textural variation in the interpretation of mechanical and transport behavior.

The mismatch observed between predicted and measured strain rates, derived from different segmentation methods, suggests two possible explanations: deformation may be primarily governed by the finer-grained matrix fraction, with larger grains acting as inert components contributing little to strain; and/or visual grain size estimates based on slab or CT data may overestimate the actual average grain size due to limitations in resolution and segmentation accuracy.

Permeation behavior appears to be modulated by microstructural features such as mega-grains, second-phase dust, and mechanical stratigraphy, all of which influence the effectiveness of grain boundary healing and the development of fluid pathways.

These findings emphasize the need for multi-scale characterization when evaluating the mechanical and hydraulic performance of rock salt. Future work involving digital twin simulations will be instrumental in disentangling the coupled effects of grain size distribution, microstructural heterogeneity, and local stress conditions on both creep and fluid transport phenomena.

Acknowledgements

The authors would like to acknowledge the IfG – Institut für Gebirgsmechanik in Leipzig, Germany, and in particular the contributions of Johannes Herrmann and Christopher Rölke for their support in preconditioning the creep samples, as well as for their valuable advice and execution of the permeation tests. This research was made possible through funding provided by Nobian Industrial Chemicals B.V., The Netherlands.

References

Andrä, H., Combaret, N., Dvorkin, J., Glatt, E., Han, J., Kabel, M., Keehm, Y., Krzikalla, F., Lee, M., Madonna, C., Marsh, M., Mukerji, T., Saenger, E.H., Sain, R., Saxena, N., Ricker, S., Wiegmann, A., Zhan, X. (2013a). Digital rock physics benchmarks—Part I: Imaging and segmentation. Comput. Geosci. 50, 25–32.

Andrä, H., Combaret, N., Dvorkin, J., Glatt, E., Han, J., Kabel, M., Keehm, Y., Krzikalla, F., Lee, M., Madonna, C., Marsh, M., Mukerji, T., Saenger, E.H., Sain, R., Saxena, N., Ricker, S., Wiegmann, A., Zhan, X. (2013b). Digital rock physics benchmarks—part II: Computing effective properties. Comput. Geosci. 50, 33–43.

Barabasch, J., Schmatz, J., Klaver, J., Schwedt, A., and Urai, J. L.(2023). Large grain-size-dependent rheology contrasts of halite at low differential stress: evidence from microstructural study of naturally deformed gneissic Zechstein 2 rock salt (Kristallbrockensalz) from the northern Netherlands, Solid Earth, 14, 271–291

Baumann, T. S., Bérest, P., Brouard, B., ter Braack, M., den Hartogh, M., Kaus, B., Klaver, J., Oonk, P., Popov, A., Schmatz, J., Urai, J. L., Wijermars, E. (2022b). CCC-integrated mul-tiscale study of salt cavern abandonment in the Netherlands. The Mechanical Behavior of Salt X, 567-576.

Baumann, T.S., Kottwitz, M.O., Popov, A.A., Schmatz, J., Brouard, B., Bakker, R.R., den Hartogh, M. (2025, this issue). 3D THM-Coupled Simulations of Low-Stress Creep Experiments Using Digital Twins of Heterogeneous Rock Salt. SMRI Spring 2025 Conference, Wilhelmshaven, Germany, 27-29 April 2025.

Bérest, P., Gharbi, H., Brouard, B., Hofer, G., Stimmisher, S., Bruckner, D., Devries, K., Hévin, G., Spiers, C.J., Urai, J. 2017. SMRI Research Report RR2017-1: Very Slow Creep Tests as a Basis for Cavern Stability Analysis.

Bérest, P., Gharbi, H., Brouard, B., Brückner, D., Devries, K., Hévin, G., Hofer, G., Spiers, C., Urai, J.L. 2019. Very Slow Creep Tests on Salt Samples. Rock Mechanics and Rock Engineering, 52(9), pp. 2917–2934.

Bérest, P., Gharbi, H., Gordeliy E., Jehanno, D., Peach, C., Brouard, B., Blanco-Martin, L. (2022). Creep tests on salt samples performed at very small stresses. Proc. SMRI Spring Meeting, Rapid City, SD, USA.

Breiman, L. (2001). Random Forests. Machine Learning 45, 5–32.

Herrmann, J., Schmatz, J., Bakker, R., Rölke, C., Naumann, D. (in press). The hydraulic properties of rock salt at elevated thermodynamic boundary conditions and its healing potential. 11th Conference on the Mechanical Behavior of Salt (SaltMech XI), July 8 – 10, 2025, Santa Fe, NM, USA.

Houben, M.E., ten Hove, A., Peach, C. J., & Spiers C.J., (2013). Crack healing in rocksalt via diffusion in adsorbed aqueous films: Microphysical modelling versus experiments. Physics and Chemistry of the Earth, Parts A/B/C, Vol 64 pp.95-104.

Ji, Y., Spiers, C.J., Hangx, S.J.T., de Bresser, J.H.P, Drury, M.R. (2022). Proceedings Of The 10th Conference on the Mechanical Behavior of Salt (Saltmech X), Utrecht, The Netherlands, 06-08 July 2022.

Kottwitz, M.O., Baumann, T.S., Schmatz, J., Popov, A.A., Brouard, B., Bakker, R.R. (in press). 3D THM-Coupled Simulations of Low-Stress Creep Experiments Using Digital Twins of Heterogeneous Rock Salt. 11th Conference on the Mechanical Behavior of Salt (SaltMech XI), July 8 – 10, 2025, Santa Fe, NM, USA.

Kozlov, E.V., Zhdanov, A.N. & Koneva, N.A. (2006). Barrier Retardation of Dislocations. Hall-Petch Problem, Phys. Mesomech., vol. 9, no. 3–4, pp. 75–85.

Küster, Y., Leiss, B., and Schramm, M. (2008). Structural characteristics of the halite fabric type ‘Kristallbrocken’ from the Zechstein Basin with regard to its development, Int. J. Earth Sci, 99, 505–526.

Li, Z., Suo, J., Fan, J., Fourmeau, M., Jiang, D., Nelias, D. (2023). Damage evolution of rock salt under multilevel amplitude creep–fatigue loading with acoustic emission monitoring. Int. J. Rock Mech. Min. Sci. 164, 105346.

Ma, W., Yang, Y., Yang, W., Lv, C., Yang, J., Song, W., Sun, H., Zhang, L., Zhang, K., Yao, J., 2023. Digital Rock Mechanical Properties by Simulation of True Triaxial Test: Impact of Microscale Factors. Geotechnics 3, 3–20.

Manthei, G. (2005) Characterization of Acoustic Emission Sources in a Rock Salt Specimen under Triaxial Compression. Bull. Seismol. Soc. Am. 95, 1674–1700.

Paterson, M. S., & Wong, T. F. (2005). Experimental rock deformation: the brittle field (Vol. 348). Berlin: Springer.

Popp, T., Minkley, W., Wiedemann, M., & Salzer, K. (2015). Gas-pressure-induced integrity of salt formations. Geological Society, London, Special Publications, 415(1), pp.107-122.

Schmatz, J., Bakker, R.R., Hermann, J., Wellmann, E., Rölke, C. Naumann, D., Jiang, M., Klaver, J., den Hartogh, M. (2024). Microstructural Investigation of Heterogeneous Rock Salt Permeation: Unraveling the influence of Anhydrite and Mega-Grain content on Fluid Transport. SMRI Spring Conference, Krakow, Poland, 22-23 April 2024.

Schmatz, J., Brouard, B., Baumann, T.S., Gharbi, H., Bakker, R.R. (in press). Microstructural Evolution of Natural Rock Salt Under Low Deviatoric Stress. 11th Conference on the Mechanical Behavior of Salt (SaltMech XI), July 8 – 10, 2025, Santa Fe, NM, USA.

Spiers C.J., Schutjens P.M.T.M., Brzesowsky R.H., Peach C.J., Liezenberg J.L., Zwart H.J. 1990. Experimental determination of the constitutive parameters governing creep of rocksalt by pressure solution. The Geological Society, London, England. 54, 215-227.

Schwichtenberg, B., Fusseis, F., Butler, I. B., And Andò, E. 2022. Biotite supports long-range diffusive transport in dissolution–precipitation creep in halite through small porosity fluctuations, Solid Earth, 13, 41–64.

Ter Heege, J.H., De Bresser, J.H.P., Spiers, C.J. 2005. Rheological behaviour of synthetic rocksalt: the interplay between water, dynamic recrystallization and deformation mechanisms, Journal of Structural Geology, Volume 27, 6, 948-963.

Thiemeyer, N., Habersetzer, J., Peinl, M., Zulauf, G. & Hammer, J. (2015) The application of high-resolution X-ray computed tomography on naturally deformed rock salt: Multi-scale investigations of the structural inventory. J. Struct. Geol. 77, 92–106.

Underwood, E.E., 1970, Quantitative Stereology, 2nd ed., Addison-Wesley Publishing Company, Reading, MA.

Urai, J. L., Spiers, C. J., Zwart, H. J., & Lister, G. S. (1986). Weakening of rock salt by water during long-term creep. Nature, 324(6097), 554–557.

Urai, J. L., Spiers, C. J., Peach, C. J., Franssen, R. C. M. W., and Liezenberg, J. L. (1987): Deformation mechanisms operating in naturally deformed halite rocks as deduced from microstructural investigations, Geol Mijnbouw, 66, 165–176.

Urai, J. L., Schmatz, J. & Klaver, J., (2019). Over-pressured salt solution mining caverns and leakage mechanisms. Phase 1 Micro-Scale Report.

Zhang, Q., Liu, J., Wang, L., Luo, M., Liu, H., Xu, H., Zou, H. (2020). Impurity Effects on the Mechanical Properties and Permeability Characteristics of Salt Rock. Energies 13, 1366.